

# An investigation of time–frequency domain phase-weighted stacking and its application to phase-velocity extraction from ambient noise’s empirical Green’s functions

Guoliang Li,<sup>1</sup> Fenglin Niu,<sup>1,2</sup> Yingjie Yang<sup>3</sup> and Jun Xie<sup>4</sup>

<sup>1</sup>State Key Laboratory of Petroleum Resource and Prospecting, and Unconventional Gas Institute, China University of Petroleum at Beijing, Beijing 102249, China. E-mail: [niu@rice.edu](mailto:niu@rice.edu)

<sup>2</sup>Department of Earth Science, Rice University, 77005 Houston, TX, USA

<sup>3</sup>Australian Research Council Centre of Excellence for Core to Crust Fluid Systems and GEMOC, and Department of Earth and Planetary Science, Macquarie University, North Ryde, NSW 2109, Australia

<sup>4</sup>Institute of Geodesy and Geophysics, Chinese Academy of Sciences, Wuhan 430077, China

Accepted 2017 October 13. Received 2017 October 10; in original form 2016 December 23

## SUMMARY

The time–frequency domain phase-weighted stacking (tf-PWS) technique based on the  $S$  transform has been employed in stacking empirical Green’s functions (EGFs) derived from ambient noise data, mainly due to its superior power in enhancing weak signals. Questions such as the induced waveform distortion and the feasibility of phase-velocity extraction are yet to be thoroughly explored. In this study, we investigate these issues by conducting extensive numerical tests with both synthetic data and USArray transportable array (TA) ambient noise data. We find that the errors in the measured phase velocities associated with waveform distortion caused by the tf-PWS depend largely on the way of how the inverse  $S$  transform (IST) is implemented. If frequency IST is employed in tf-PWS, the corresponding errors are generally less than 0.1 per cent, sufficiently small that the measured phase velocities can be safely used in regular surface wave tomography. On the other hand, if a time IST is used in tf-PWS, then the extracted phase velocities are systematically larger than those measured from linearly stacked ones, and the discrepancy can reach as much as  $\sim 0.4$  per cent at some periods. Therefore, if tf-PWS is used in stacking EGFs, then frequency IST is preferred to transform the stacked  $S$  spectra back to the time domain for the stacked EGFs.

**Key words:** Time-series analysis; Seismic noise; Seismic tomography; Surface waves and free oscillations.

## 1 INTRODUCTION

In seismology, extracting weak signals from noisy records, such as reflected and scattered waves at Earth’s internal structures, is a challenging task with great importance. In particular, raising signal-to-noise ratio (SNR) of interstation empirical Green’s functions (EGFs), which are the negative time derivatives of noise correlation functions (NCFs), has significant implications in better constraining crustal and upper-mantle velocity structures (e.g. Shapiro *et al.* 2005; Yang *et al.* 2007; Lin *et al.* 2014; Li *et al.* 2016), as well as in detecting temporal changes of the subsurface velocity field (e.g. Grêt *et al.* (2005); Sens-Schönfelder & Wegler 2006; Breguier *et al.* 2008; Cheng *et al.* 2010). Linear stacking is the classic technique to enhance weak signals, which can improve the SNR by a factor of  $N^{1/2}$  (here,  $N$  refers to the number of traces in stacking of cross-correlation) when the noise among EGFs is uncorrelated. This means that a significant amount of temporal stacking of NCFs is required in order to obtain high-quality EGFs, which are essential

for extracting body wave phases, as well as for detecting temporal changes of the subsurface velocity field. Thus, there is a great demand for exploring new stacking algorithms that can achieve efficiency better than  $N^{1/2}$ , and yet retain the waveform shapes as much as possible. The latter is important in correctly extracting phase velocities from EGF data.

In fact, several non-linear stacking methods that demonstrate better stacking efficiency have been proposed by a number of previous studies, for example, the  $n$ th root stacking (Muirhead 1968; Kanasewich *et al.* 1973), the phase-weighted stacking (PWS, Schimmel & Paulssen 1997), and the time–frequency domain phase-weighted stacking (tf-PWS, Schimmel & Gallart 2007). The  $n$ th root stacking takes account of both amplitudes and cross-correlation of the time sequences, therefore, it is more efficient in reducing uncorrelated noise as compared to the regular linear stack. The choice of the power  $n$  in the  $n$ th root stacking is somewhat subjective, and generally a larger  $n$  leads more distortion in the stacked waveform. The PWS technique also introduces coherence in enhancing signals,

which generally shows a smaller waveform distortion than the  $n$ th root stacking (Schimmel & Paulssen 1997). It employs the differences among the instantaneous phases of the time sequences as the coherence index to weight the linear stack, and small differences in the instantaneous phases mean a high weighting factor. The linearly stacked trace is then weighted by a function calculated from the instantaneous phase of each channel. Because of the waveform distortion involved in these two stacking methods, they are mainly used in identifying weak body wave phases.

Similar to the PWS, the tf-PWS also employs a phase derived coherence function to weight the traces in the stack (Schimmel & Gallart 2007). However, the phases are the local phases computed from the  $S$  transform rather than the instantaneous phases calculated from the Hilbert transform. Stockwell *et al.* (1996) first introduced the original  $S$  transform (equivalent to  $k = 1$  in following eq. 1) to analyse geophysical data. Mansinha *et al.* (1997) further applied it to several types of geophysical data. Since then several modified versions of the  $S$  transform have been proposed for various purposes, such as the generalized  $S$  transform (GST) proposed by McFadden *et al.* (1999), the modified  $S$  transform (MST) suggested by Li & Castagna (2013) with a more flexible time windowing scheme (Kazemi *et al.* 2014). Baig *et al.* (2009) employed the discrete orthonormal  $S$  transform (Stockwell 2007) to incorporate a phase coherence filter in denoising EGFs, which allowed them to observe a clear precursor to the 2000 June eruption from le Piton de la Fournaise volcano on La Réunion Island.

One application of the  $S$  transform is for designing data-adaptive filters (Schimmel & Gallart 2005). The filtering involves a forward transform to the time–frequency domain, a modification of the localized spectrum (or elapse time spectrum), and a backward inverse  $S$  transform (IST), which transforms the time–frequency function back to the time domain. The IST is usually implemented either in the frequency domain (frequency IST, Stockwell *et al.* 1996) or in the time domain (time IST, Schimmel & Gallart 2005). Based on the amplitude spectrum of the  $S$  transform, Pinnegar & Eaton (2003) devised an adaptive filter to attenuate the noise in pre-stack seismic data. The tf-PWS method proposed by Schimmel & Gallart (2007) is another type of adaptive filtering technique. It first utilizes the  $S$  transform to compute the elapse time spectra of multichannel data, and then weights the traces composing the stack with coherence functions derived from the local phases. The stacked spectrum is finally transformed back to a time-series using the time IST method (Schimmel & Gallart 2007). Schimmel & Gallart (2007) first applied this technique to teleseismic data recorded by a broad-band seismic array in NW Spain, which reveals weak conversions/reflections at the 410- and 660-km discontinuity. Schimmel *et al.* (2011) further employed the tf-PWS technique to the extraction of EGFs from ambient noise data, which leads to the detection of body waves at a local scale and the Rayleigh waves traveling along both the minor and major arcs (i.e. the R1 and R2) at a global scale.

While it can suppress incoherent noise more efficiently than linear stacking, it is also true that tf-PWS can cause waveform distortion due to its non-linear nature. Such waveform distortion may affect the extraction of phase velocities and waveform fitting in the regular ambient noise surface wave tomography (e.g. Shapiro *et al.* 2005; Yang *et al.* 2007, 2012) and ambient noise adjoint tomography (e.g. Chen *et al.* 2014; Liu *et al.* 2017), respectively. Although there is a growing tendency to employ the tf-PWS technique to obtain EGFs from ambient noise data with less amount of temporal stacking, there are a few fundamental questions yet to be answered. For example, how accurately can we extract phase velocities from

the tf-PWS stacks; whether and how can the two types of the ISTs affect the accuracy of the extracted phase velocities; how effective is tf-PWS in raising SNR? In this study, we conduct extensive tests with both synthetic and observed EGFs derived from ambient noise data in order to answer these questions.

## 2 METHOD

### 2.1 $S$ transform

According to Stockwell *et al.* (1996), the  $S$  transform is a generalization of the short-time Fourier transform, which extends the continuous wavelet transform and overcomes some of its disadvantages. Here, we start with the GST (McFadden *et al.* 1999):

$$S(\tau, f) = \int_{-\infty}^{+\infty} u(t)w(\tau - t, f)e^{-i2\pi ft} dt, \quad (1)$$

where the elapse time spectra ( $S(\tau, f)$ ) are complex-valued functions,  $u(t)$  is a continuous time function and  $w(\tau - t)$  is a Gaussian function:

$$w(\tau - t, f) = \frac{|f|}{\sqrt{2\pi}k} e^{-\frac{f^2(\tau-t)^2}{2k^2}}, \quad k > 0. \quad (2)$$

Here, the standard deviation is  $\sigma = k/|f|$ , therefore  $k = \sigma/T$  is a parameter that controls the number of Fourier sinusoidal periods ( $T$ ) within one standard deviation of the Gaussian window ( $\sigma$ ). It is used here to balance the time and frequency resolution. Also, if  $k = 1$ , then the GST becomes the original  $S$  transform (Stockwell *et al.* 1996), and if  $k$  is a variable that varies with time or frequency, then the GST becomes the MST (Li & Castagna 2013).

Stockwell *et al.* (1996) point out that eq. (1) can be perceived as a convolution of the functions  $h(t, f) = u(t)e^{-i2\pi ft}$  and  $w(t, f)$ . The Fourier transform of the two functions can be written as:

$$\begin{aligned} H(v, f) &= \int_{-\infty}^{+\infty} \{u(t)e^{-i2\pi ft}\} e^{-i2\pi vt} dt = \int_{-\infty}^{+\infty} u(t)e^{-i2\pi(v+f)t} dt \\ &= U(v + f), \end{aligned} \quad (3a)$$

$$W(v, f) = \int_{-\infty}^{+\infty} \frac{|f|}{\sqrt{2\pi}k} e^{-\frac{f^2 t^2}{2k^2}} e^{-i2\pi vt} dt = \exp\left\{-\frac{2\pi^2 k^2 v^2}{f^2}\right\}. \quad (3b)$$

Here,  $U(v) = \int_{-\infty}^{+\infty} u(t)e^{-i2\pi vt} dt$  is the Fourier spectrum of  $u(t)$ . Therefore, the localized spectrum  $S(\tau, f)$  of the GST can be calculated from an inverse transform of the product of the two spectra:

$$\begin{aligned} S(\tau, f) &= \mathfrak{S}^{-1}[U(v + f)W(v, f)] \\ &= \int_{-\infty}^{+\infty} U(v + f) e^{-\frac{2\pi^2 k^2 v^2}{f^2}} e^{i2\pi v\tau} dv \quad f \neq 0. \end{aligned} \quad (4)$$

Eq. (4) shows that for each frequency ( $f$ ), it requires one-time inverse Fourier transform of the spectrum of the input signal ( $U(v)$ ), therefore it is a more efficient way to calculate the elapse time spectra  $S(\tau, f)$  as compared to eq. (1).

### 2.2 Time–frequency domain phase-weighted stacking

The elapse time spectra ( $S(\tau, f)$ ) can be expressed as:

$$S(\tau, f) = A(\tau, f)e^{i\Phi(\tau, f)}. \quad (5)$$

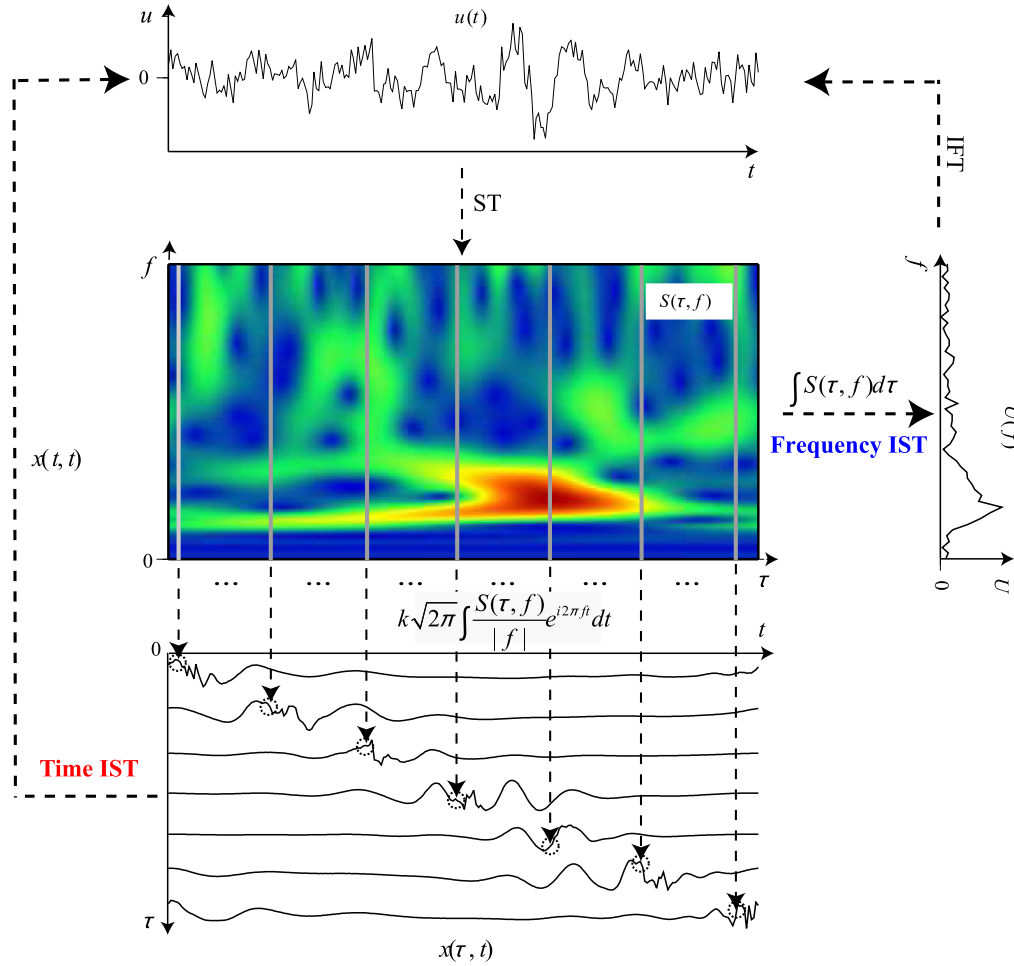


**Figure 1.** A schematic diagram showing the two ways to transform the time–frequency spectra  $S(\tau, f)$  back to the time-domain signal. The 1-D time-series  $u(t)$  are projected to 2-D time–frequency domain by  $S$  transform, known as the elapse time spectra or localized spectra  $S(\tau, f)$ . It is noteworthy that only the amplitude spectra are plotted here. Here,  $U(f)$  represents the Fourier transform of the time-series and again only its amplitude component is shown in the figure.

Here,  $A(\tau, f)$  and  $\Phi(\tau, f)$  are, respectively, the amplitude spectrum and phase spectrum of the corresponding spectrum  $S(\tau, f)$  at elapse time  $\tau$ . Schimmel & Gallart (2007) introduce a phase stack,  $c_{ps}(\tau, f)$ , which is defined as the absolute value of the complex summation of the amplitude normalized traces

$$c_{ps}(\tau, f) = \frac{1}{N} \sum_{j=1}^N e^{i\Phi_j(\tau, f)}, \quad (6)$$

here  $j$  and  $N$  are the trace index and the total number of traces, respectively.  $c_{ps}(\tau, f)$  varies from 0 to 1, which is achieved when all the traces are perfectly coherent. This coherence-dependent function with a power  $\nu$  is further used as the weight of the linear stack, which yield the tf-PWS:

$$S_{pws}(\tau, f) = |c_{ps}(\tau, f)|^\nu \frac{1}{N} \sum_{j=1}^N S_j(\tau, f). \quad (7)$$

### 2.3 Frequency and time inverse $S$ transforms

As mentioned above, there are two ways to implement the IST (Fig. 1), which are named the frequency IST and the time IST by Simon *et al.* (2007). The frequency IST algorithm (Stockwell *et al.*

1996) is rather straightforward, and can be written as:

$$u(t) = \int_{-\infty}^{+\infty} \int_{-\infty}^{+\infty} S(\tau, f) d\tau e^{i2\pi f t} df = \int_{-\infty}^{+\infty} U(f) e^{i2\pi f t} df. \quad (8)$$

Here,  $U(f)$  is the Fourier transform of  $u(t)$ . Basically, the frequency IST first collapses the local spectrum into a regular Fourier spectrum by an integral in the elapse time domain. The time-series  $u(t)$  is then recovered by one regular inverse Fourier transform of the collapsed spectrum. It can be shown that the modified elapse spectra  $S(\tau, f)$  by the tf-PWS defined in eq. (7) only change the amplitude, not the phase of time sequence if the frequency IST equation (8) is used (Appendix).

The time IST is introduced by Schimmel & Gallart (2005). They first define an elapse time–time function (for any fixed frequency  $f$ ):

$$x(\tau, t) = u(t) e^{-\frac{f^2(\tau-t)^2}{2k^2}}. \quad (9)$$

Obviously,  $x(t, t) = u(t)$ . They further find that its Fourier spectrum  $X(\tau, f)$  is related to the elapse time spectrum  $S(\tau, f)$  through the following equation:

$$X(\tau, f) = \int_{-\infty}^{+\infty} x_f(\tau, t) e^{-i2\pi f t} dt = \frac{\sqrt{2\pi}k}{|f|} S(\tau, f). \quad (10)$$

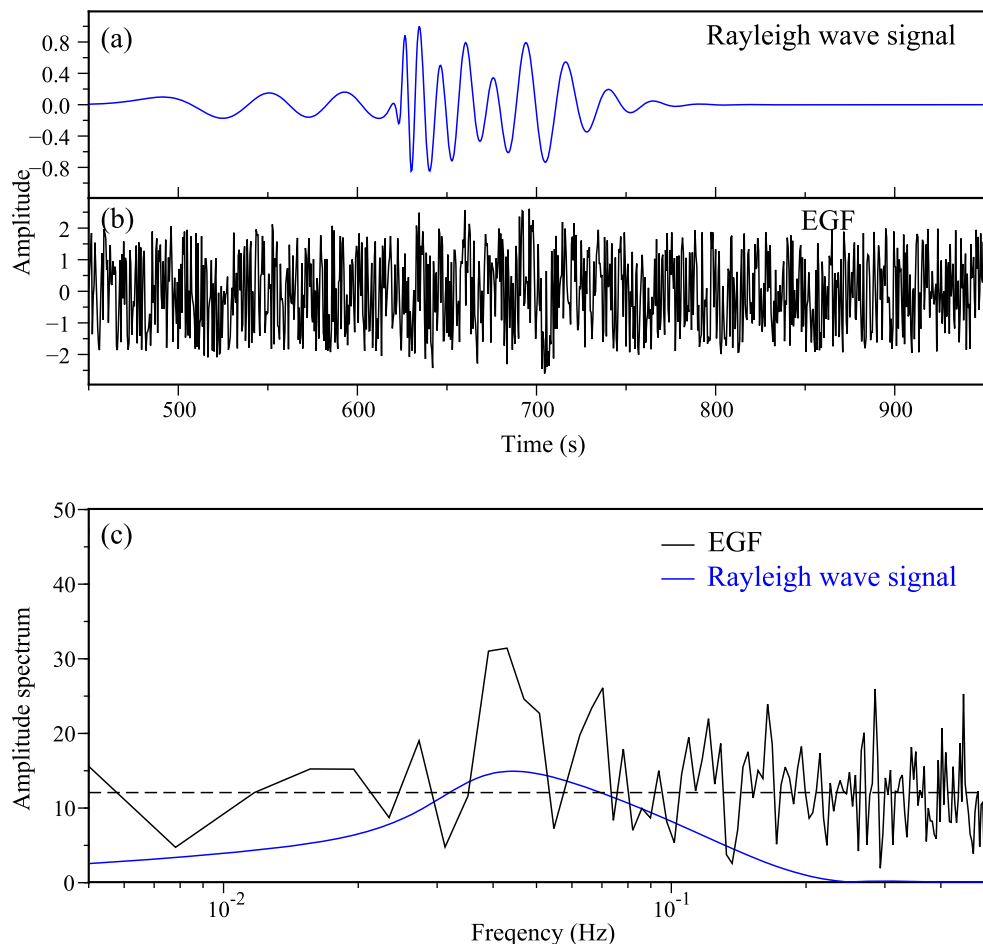


**Figure 2.** (a) Two examples showing a fundamental Rayleigh wave signal recorded at 2000 km and (b) a synthetic EGF with large uncorrelated noise. Their corresponding amplitude spectra are shown in (c) with the blue and black lines representing the Rayleigh wave signal and the EGF, respectively. The dashed line in (c) is the average amplitude spectrum of the EGF.

Therefore,  $u(t)$  can be achieved from the weighted  $S$  spectrum by taking the diagonal elements of the elapse time–time function,  $x(\tau, t)$ , which is calculated with an inverse Fourier transform:

$$u(t) = x(t, t) = \sqrt{2\pi k} \int_{-\infty}^{+\infty} \frac{S(t, f)}{|f|} e^{2i\pi f t} df. \quad (11)$$

According to Schimmel & Gallart (2005), the merit of this algorithm is that any modifications of the elapse time spectra  $S(\tau, f)$  can be directly translated to the filtered time-series, which implies better time localization. In other words, if we change the spectra  $S(\tau, f)$  at a certain elapse time, this will lead to a direct change of  $u(t)$  at the given time based on the time IST equation (11). However, if we use the frequency IST equation (8), the given time information is wiped out by the integration over the elapse time, which leads to a modification in the Fourier spectrum  $U(f)$ . It is not so obvious to link to spectrum change with the given time. If  $S(\tau, f)$  is not modified, then  $u(t)$  can be perfectly recovered by eq. (11) (Schimmel & Gallart 2007). On the other hand, if  $S(\tau, f)$  is modified by certain filtering schemes, such as tf-PWS, then the recovered time sequence generally shows some degree of distortion (Appendix).

### 3 SYNTHETIC TESTS

We begin our presentation with results from numerical tests of synthetic EGFs, which are designed to quantify the effect of tf-PWS

on the accuracy of phase-velocity extraction and the efficiency in SNR enhancement. We also investigate how the two types of IST affect the estimate of phase velocities from the synthetic EGFs. In all the tests, we set the power  $\nu$  in eq. (7)–(1). We have also tried the commonly used  $\nu = 2$  and found that it leads more severe waveform distortion. Therefore, it seems that  $\nu = 1$  is an appropriate choice in balancing the coherence weighting and linear stacking to produce the final stacking results.

#### 3.1 Accuracy in phase-velocity extraction

We employ the Computer Programs in Seismology of Herrmann & Ammon (2004) to generate a synthetic fundamental Rayleigh wave with a period range of  $\sim 5$ –200 s recorded at an epicentral distance of 2000 km (Fig. 2a). The signal of the fundamental Rayleigh wave falls in a time window from 500 to 1000 s. The sample rate of the seismic waveform is two samples per second. We mix this Rayleigh wave signal with random noise sequences to represent synthetic EGFs, which are intended to be the mimics of the daily EGFs in ambient noise studies. To generate the random noise series, we first take the maximum absolute amplitude ( $R_{\max}$ ) of the Rayleigh wave signal, which equals 1 in our case. We then generate uniformly distributed random numbers, and further scale them to the amplitude range of  $-2R_{\max}$  to  $2R_{\max}$ . We generate a total of 30 sets of data with each containing 365 daily EGFs, representing one year of ambient

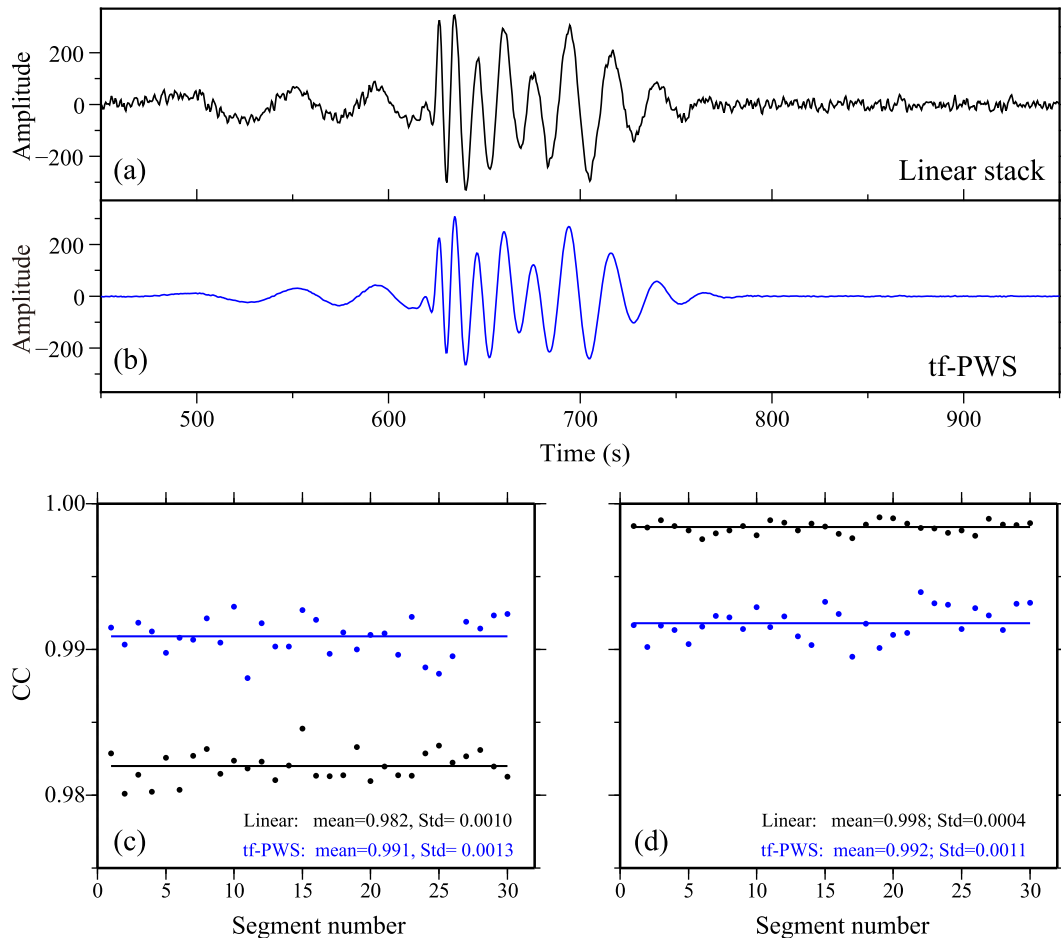


**Figure 3.** Two examples showing (a) the stacked EGFs constructed with linear stacking and (b) frequency IST based tf-PWS, respectively. The cross-correlation coefficients between the 30 sets of stacked EGFs and the Rayleigh wave signal shown in Fig. 2(a) are shown in (c), with black and blue corresponding to the linear and tf-PWS stacks, respectively. (d) Same as (c) except that the EGFs are bandpass filtered in 10–100 s.

noise data. An example of a daily EGF is plotted in Fig. 2(b), which shows that the Rayleigh wave signal is completely hidden inside the noise. In Fig. 2(c), we show the amplitude spectra of the daily EGF and the Rayleigh wave signal in black and blue lines, respectively. It is clear that the amplitude of the EGF is larger than the Rayleigh wave signal in most of the frequency band (Fig. 2b). We have also tried noise series that follow the Gaussian distribution and found that the results remain the same.

For each set of the EGF data that contains a total of 365 individual EGFs, we employ the frequency IST based tf-PWS to generate a stacked EGF, which is used to extract phase velocities. For comparison, we also generate a linear stack from the 365 EGFs. Figs 3(a) and (b) show the stacked EGFs of one set of 365 individual EGFs that are constructed from the linear stacking and tf-PWS methods, respectively. In general, the Rayleigh wave signal is clearly shown in both stacks, and the noise level in the tf-PWS trace is much lower than that in the linear stack (Figs 3a and b). In order to quantify the similarity between the stacked waveforms and the original Rayleigh wave signal, we use the Rayleigh wave signal as the reference and compute the cross-correlation coefficients (CCs) between the reference and stacked waveforms. When computing the CCs, we select the Rayleigh wave arrival time window between 550 and 800 s. The computed CCs of the stacks from the 30 data sets are shown in Fig. 3(c). Both types of stacks show very high CCs with an average value of 0.982 for the linear stack and 0.991 for the tf-PWS (Fig. 3c).

Here, we do not apply any filtering to the stacked waveforms. The high CCs from the tf-PWS suggest that the waveform distortion induced by the non-linear stacking is very minor. Also the slightly lower CCs of the linear stack are likely caused by the high-frequency noise overprinted on the Rayleigh wave signal (Fig. 3a). This becomes clear when we filter the stacked waveforms with a bandpass filter between 10 and 50 s, which is the dominant period band of the Rayleigh wave signal (Fig. 2c). We then recomputed the CCs between the bandpass filtered stacks and the reference trace, which are shown in Fig. 3(d). As compared to Fig. 3(c), the average CC calculated from the linear stacks increases significantly from 0.982 to 0.998. In contrast, the average CC from tf-PWS remains more or less the same (from 0.991 to 0.992). Moreover, the CCs from the bandpass filtered data show that the tf-PWS stacks generally have lower CCs than the linear stacks do, suggesting that a minor degree of waveform distortion has indeed been introduced by the non-linear tf-PWS method.

Since the fundamental Rayleigh wave shown in Fig. 2(a) is recorded at an epicentral distance of 2000 km, therefore we know the exact values of its phase and group velocities, which we can use for calibrating the measured phase and group velocities from the stacked EGFs. We employ the frequency–time analysis (FTAN) method (e.g. Dziewonski *et al.* 1969; Herrin & Goforth 1977; Levshin & Ritzwoller 2001) to extract the group and phase velocities from the stacked EGFs. The average group and phase velocities

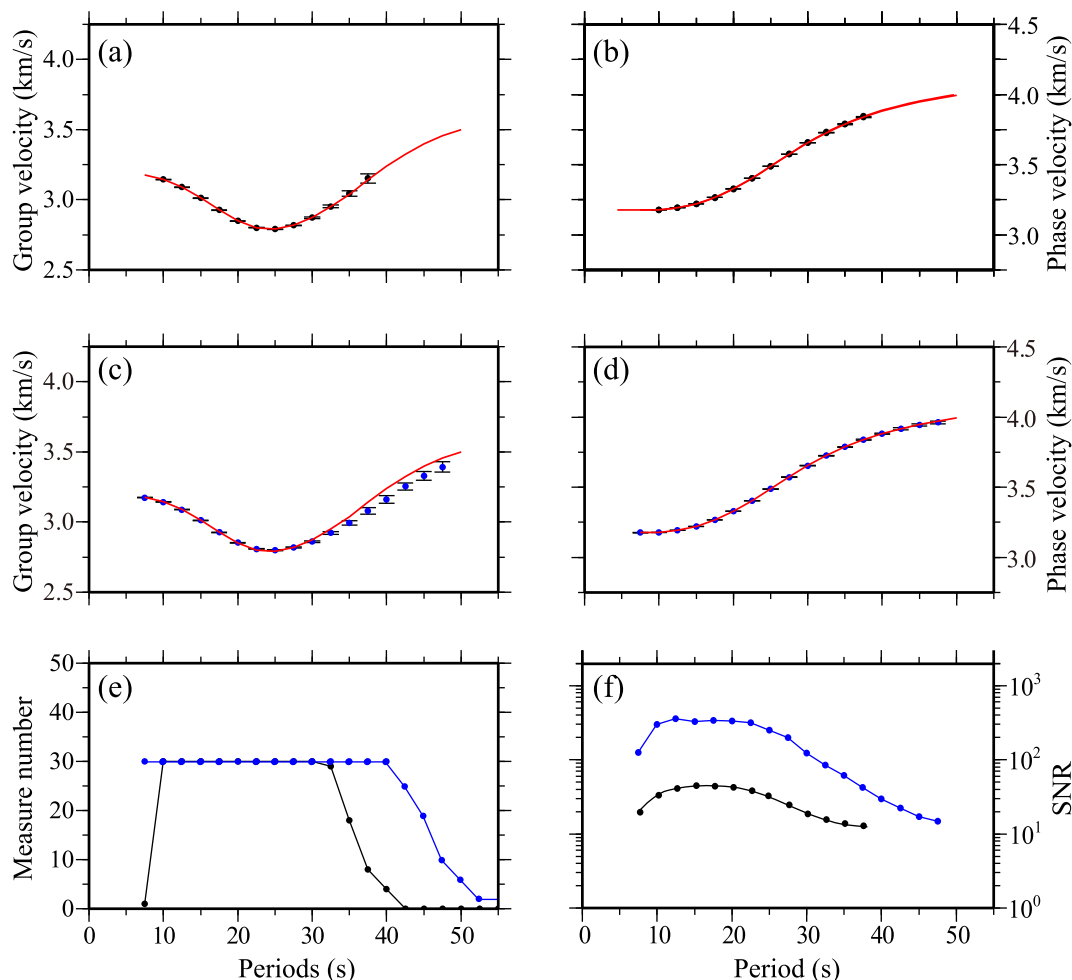


**Figure 4.** The group and phase velocities measured at periods from 5 to 60 s averaged from the 30 sets of linearly stacked EGFs, together with the standard deviations, are shown in (a) and (b), respectively. The red lines in (a) and (b) represent the true group and phase velocities of the Rayleigh wave signal shown in Fig. 2(a). (c) and (d) are the same as (a) and (b) except that the EGFs are generated by the frequency IST-based tf-PWS method. The numbers of effective measurements (see the main text for definition) from the 30 sets of EGFs (e) and the average SNRs (f) are shown as a function of period, with black and blue corresponding to the linear and tf-PWS stacks, respectively.

with their standard deviations measured from the linear and tf-PWS stacks are shown in Figs 4(a) and (b), and (c) and (d), respectively. For comparison, in each figure we also show the exact group/phase velocities with a red line. For each period, the measurement is regarded as an effective one only when the SNR is greater than 10 (Bensen *et al.* 2007). Also, only when there are more than six measurements from the total 30 stacks, we compute the averaged group or phase velocities of this period. In Figs 4(e) and (f), we show the number of effective measurements from the linear (black dots) and tf-PWS (blue dots) stacks, and the average SNR at each period.

It is clear that we can obtain more effective measurements at the two ends of the period band from the tf-PWS stacks (Fig. 4e). For the linear stacking, the number of effective measurements drops dramatically at periods less than 10 s and greater than 32.5 s (black dots in Fig. 4e). In contrast, the number from the tf-PWS stacks begins to drop only at periods greater than 40 s (blue dots in Fig. 4e). As a result, we have more measurements of the phase and group velocities from the tf-PWS stacks (Figs 4a–d). The average SNRs of the tf-PWS stacks are also much higher than those of the linear stacks (Fig. 4f).

Overall, the phase-velocity measurements fall on the reference line, whereas the group velocities at long periods measured from the

tf-PWS stacks appear to be slightly lower than the true values. The largest difference is less than  $0.06 \text{ km s}^{-1}$ , equivalent to  $\sim 2$  per cent. This suggests that the waveform distortion caused by tf-PWS does affect group velocity measurements, but the effect is generally not so significant. On the other hand, the distortion seems to have a negligible effect on the phase-velocity measurements if frequency IST is employed in the stacking.

### 3.2 Comparison of SNR enhancement between linear stacking and tf-PWS

To compare the efficiency for raising SNR between linear stacking and tf-PWS, we again use the synthetic EGFs generated in the previous subsection. First, we define the SNR as the ratio between the largest amplitude of a signal ( $A_s$ ) to the root mean square (rms) of the noise ( $\sigma_n$ ), that is,  $\text{SNR} = A_s/\sigma_n$ . Since the maximum amplitude of the signal is determined, we focus on how the rms of noise decays with increasing number of traces used in the stacking.

As mentioned above the random noise is uniformly distributed numbers varying between  $-2$  and  $2$  with an expected rms value of  $\sim 1.15$  ( $2/\sqrt{3}$ ). We choose a series of numbers  $N$  ( $N = 2^2, 3^2, \dots, 16^2$ ) to stack the noise segments using the linear stacking and the

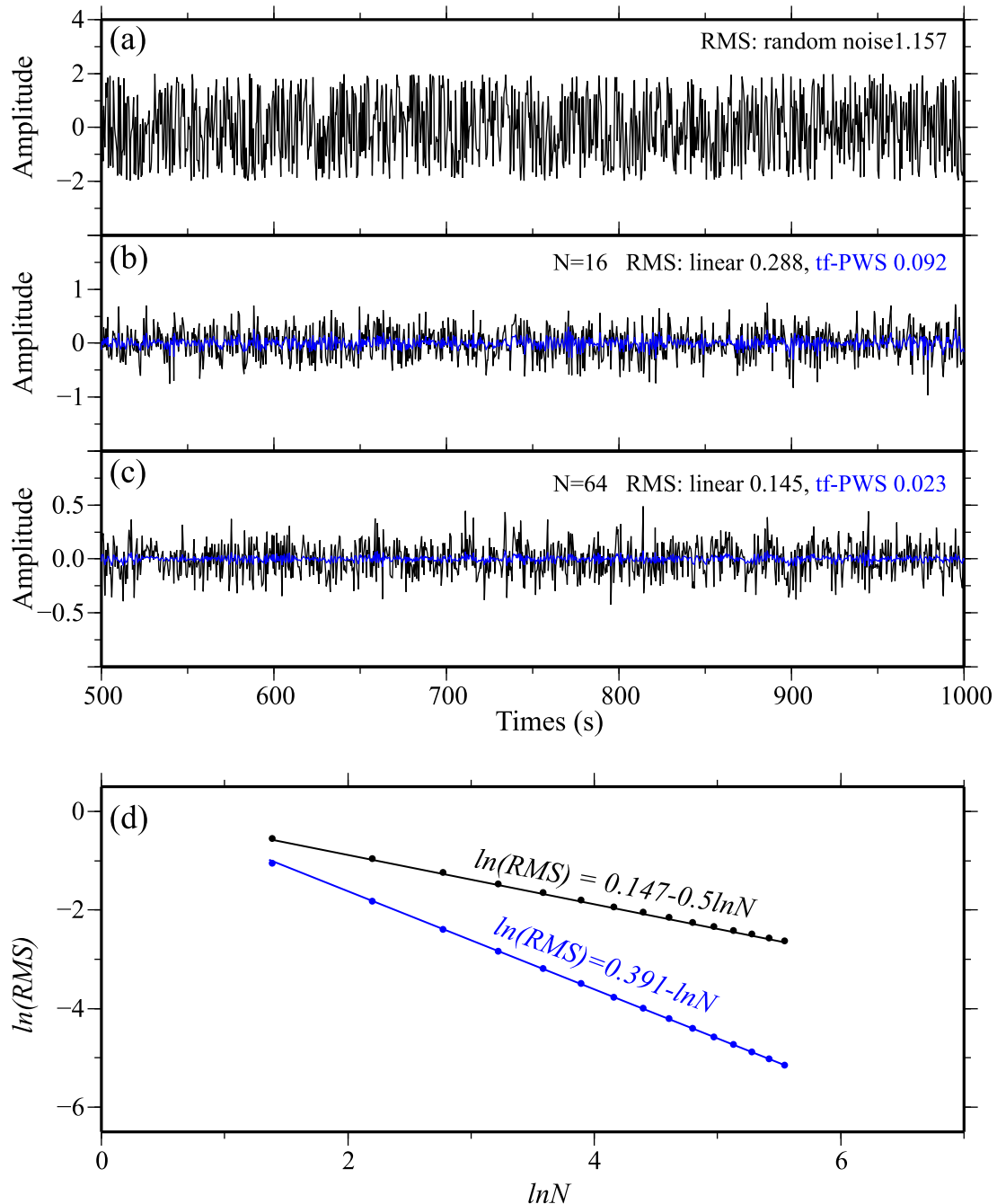


**Figure 5.** An example of the noise segments (a) is plotted with two examples of the stacked noise segments with stack number of 16 (b) and 64 (c). The linear and frequency IST-based tf-PWS stacks are shown in black and blue, respectively. (d) The measured root mean square (rms) of the stacked noise segments is shown as a function of the number of segments used in stacking. Natural logarithm is used for both axes. Black and blue dots correspond to the linear and tf-PWS stacks, respectively. Note the fast decay of rms of the tf-PWS stacks.

frequency IST-based tf-PWS. One example of the noise segment and two examples of the normalized stacked segments (normalized by  $N$ ) with  $N = 16$  and 64 are shown in Figs 5(a), and (b) and (c), respectively. After stacking, we measure the  $\sigma_n$  of all the stacked segments, which are shown in Fig. 5(d). It is clear that  $\sigma_n$  is a linear function of  $N^{-1/2}$  for the linear stacks and  $N^{-1}$  for the tf-PWS stacks. As a result, the SNR increases by a factor  $N^{1/2}$  for linear stacking and by  $N$  for the tf-PWS.

We further apply narrow bandpass Gaussian filters (Hermann 1973; Levshin *et al.* 1989) to obtain EGFs at periods of 10, 20 and 30 s and then stack them for SNR measurement. The measured

SNRs from the stacked EGFs at periods of 10, 20 and 30 s are shown in Fig. 6. It is noteworthy that the horizontal axes in Figs 6(a)–(c) are the square root of the number of stacked times ( $N^{1/2}$ ). On the other hand, the horizontal axes in Figs 6(d)–(f) are the number of traces used in stacking ( $N$ ). We apply a linear regression technique to all the SNRs, which are shown as the straight lines in Fig. 6. For the linear stacking, the slopes of the straight lines are 1.62, 1.98 and 1.04 for periods of 10, 20 and 30 s, respectively. They represent the SNRs when  $N = 1$ , which means that they are the averaged SNRs of all the individual EGFs. We further confirm this from the narrowly bandpass filtered traces of the EGF shown in Fig. 2(b).

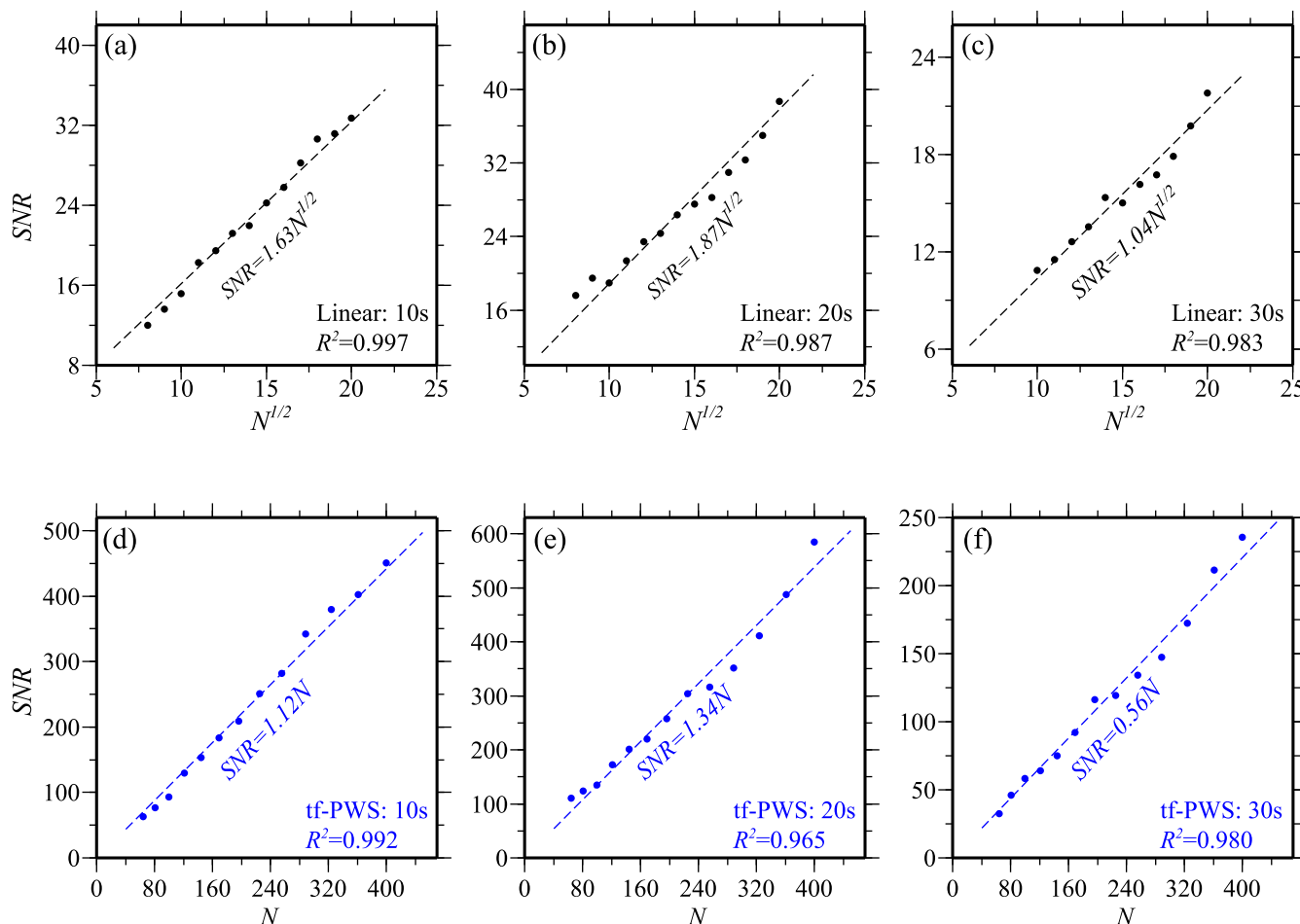


**Figure 6.** The measured average SNR measured from the linearly stacked EGFs at periods of (a) 10 s, (b) 20 s and (c) 30 s is shown as a function of the square root of the number of stacks. The dashed line in each plot is the linear fitting derived from the linear regression technique, the coefficient of determination,  $R^2$ , which measures the goodness of the linear fitting and equals 1 for a perfect fitting, is also shown. (d)–(f) are the same as (a)–(c) except for that the EGFs are constructed with the frequency IST-based tf-PWS method, and the horizontal axes are the number of traces used in stacking, not the square roots.

For the tf-PWS stacks, we obtain a slope of 1.12, 1.34 and 0.56 for the three periods, respectively. Since the SNR of the tf-PWS is proportional to  $N$ , the tf-PWS can achieve SNRs higher than those of the linear stacking with the same amount stacking (on average by a factor related to  $N^{1/2}$ ). This is desirable for the detection of body waves, which usually have lower SNRs as compared to the surface waves. Also in the application of using EGFs to detect temporal velocity changes of the subsurface medium, this means high temporal resolution as we can obtain high-quality EGFs with less temporal stacking.

### 3.3 A comparison of the time and frequency ISTs

We further investigate the potential difference between the frequency and time IST selected in performing the tf-PWS. To do so, we expand the number of EGFs from 365 to 730 in each of the 30 data sets generated in Section 3.1. The large numbers are required in order to obtain phase velocities at long periods. For each data set, we first produce two tf-PWS stacks using the frequency and time ISTs, and then extract the phase velocities from the stacked EGFs using the FTAN method. Finally, we average the measured phase velocities from the 30 data sets.

In Fig. 7(a), we show the deviations of the measured phase velocities from true values (open circles with solid lines). In general, the

frequency IST-based phase velocities (open black circles) possess much smaller deviations than those derived from the time IST (open red circles). In particular, the deviation derived from the time IST-based tf-PWS stacks starts to increase at 30 s period and reaches the maximum value at 70 s period; it then slightly decreases at periods longer than 80 s (open red circles and red line in Fig. 7a). Note that this systematic deviation is observed from all the 30 synthetic data sets, and the measured phase velocities are always higher than the true values. Assuming an average phase velocity of  $4 \text{ km s}^{-1}$  at the 60 s period and an epicentral distance of 4000 km, the traveltime of the 60-s Rayleigh wave is 1000 s. Therefore, a 0.4 per cent deviation means a 4 s traveltime error, which could be a significant error source for surface wave tomography. On the other hand, the measurements from the frequency IST-based tf-PWS stacks are very close to the true values. Except for a peak of  $\sim 0.03$  per cent at the period of 20 s and a trough of  $\sim 0.1$  per cent at the period of 50 s, most of the deviations are close to zero (open black circles and black line in Fig. 7a).

## 4 REAL-DATA EXAMPLES

We next apply both the frequency IST-based tf-PWS and the time IST-based tf-PWS to the ambient noise data recorded by the US-Array TA stations during 2008–2012. We adopt the processing

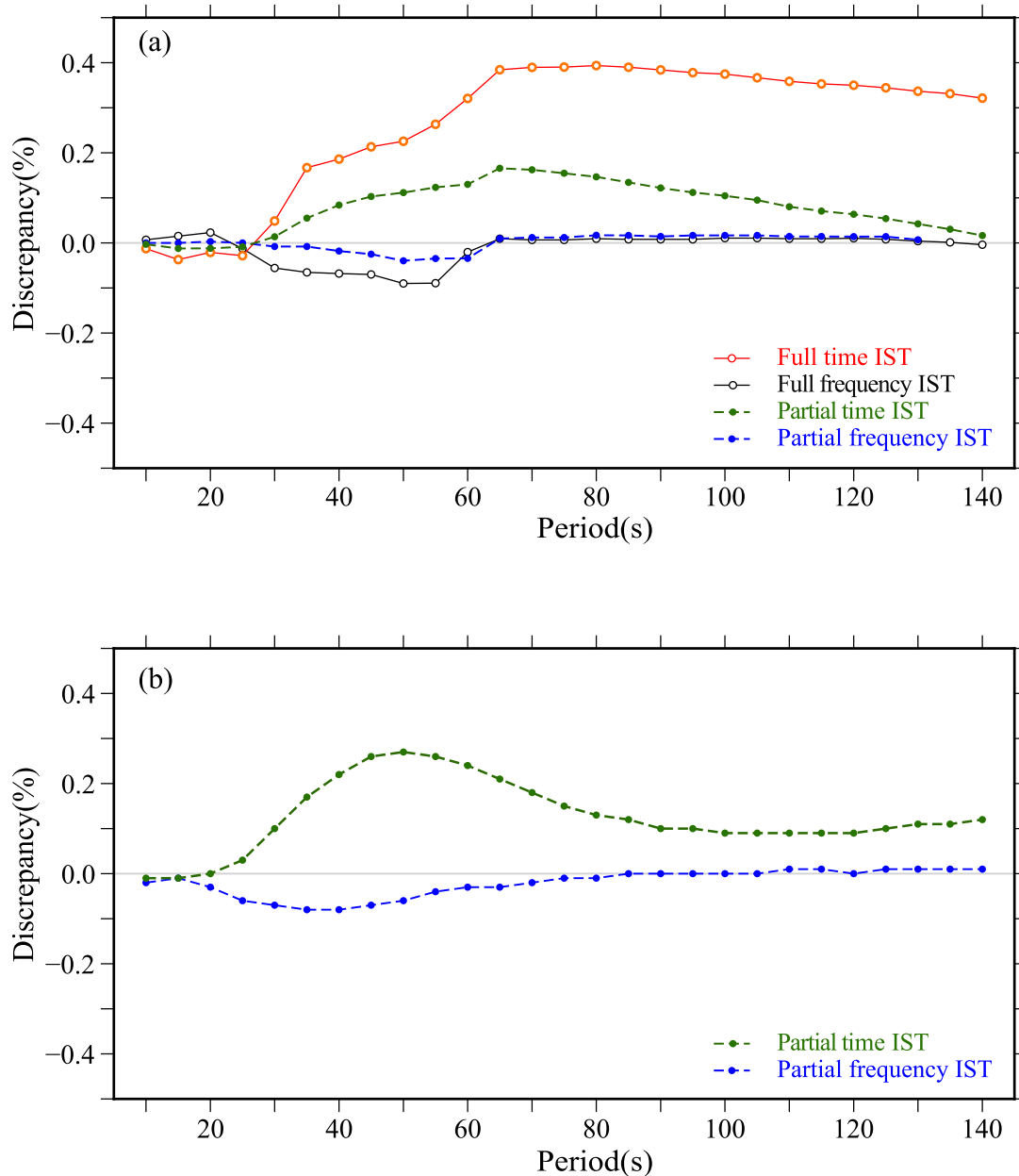


**Figure 7.** (a) Average phase-velocity deviations measured from the tf-PWS stacks of 730 daily EGFs using frequency IST and time IST are shown in open black and red circles, respectively. For comparison measurements from the partial tf-PWS stacks of 73 10-d EGFs with frequency IST and time IST are shown in blue and green dots, respectively. Note that the deviations increase with the number of non-linear stacking. (b) Average phase-velocity deviations measured from partial tf-PWS stacks of 63 10-d EGFs of the USArray noise records are shown in solid blue and green circles for the frequency and time IST implement, respectively. Note that the EGFs associated with time IST exhibit systematically higher phase velocities at long periods.

procedures proposed by Bensen *et al.* (2007) to pre-process the ambient noise data at each station and use them to compute the daily EGFs. Due to the large number of daily EGFs, we first linearly stack 10 daily EGFs to produce a single EGF. We then stack these 10-d EGFs using both the linear stacking and the two tf-PWS methods to construct three sets of stacked EGFs for phase-velocity measurement. Fig. 8 shows four examples of the linearly stacked (left) and frequency-based tf-PWS-stacked (right) EGFs computed from ambient noise data recorded at station pairs that are separated by  $\sim 500$ – $2000$  km. All the EGFs are normalized for comparison. In general, the noise levels in the tf-PWS produced EGFs shown in the right-hand column are lower than those from linear stack shown in the left-hand column.

Furthermore, we measure the phase velocities of EGFs between 10 and 140 s using the FTAN method. Only those EGFs with  $\text{SNR} > 10$  and interstation distances longer than two wavelengths are selected for the measurements of phase velocity. At each period, we compute the differences in percentage between the phase velocities measured from the two sets of tf-PWS-stacked EGFs and the linearly stacked EGFs, which are shown in Fig. 7(b). In the case of frequency IST-based tf-PWS, the biggest discrepancy is observed at periods of 35 and 40 s with a mean of 0.08 per cent, and becomes almost zero at periods longer than 60 s or smaller than 20 s (solid blue dots in Fig. 7b). On the other hand, the discrepancy between the time IST-based tf-PWS and linear stacks is close to zero at periods shorter than 20 s, but increases quickly with increasing period

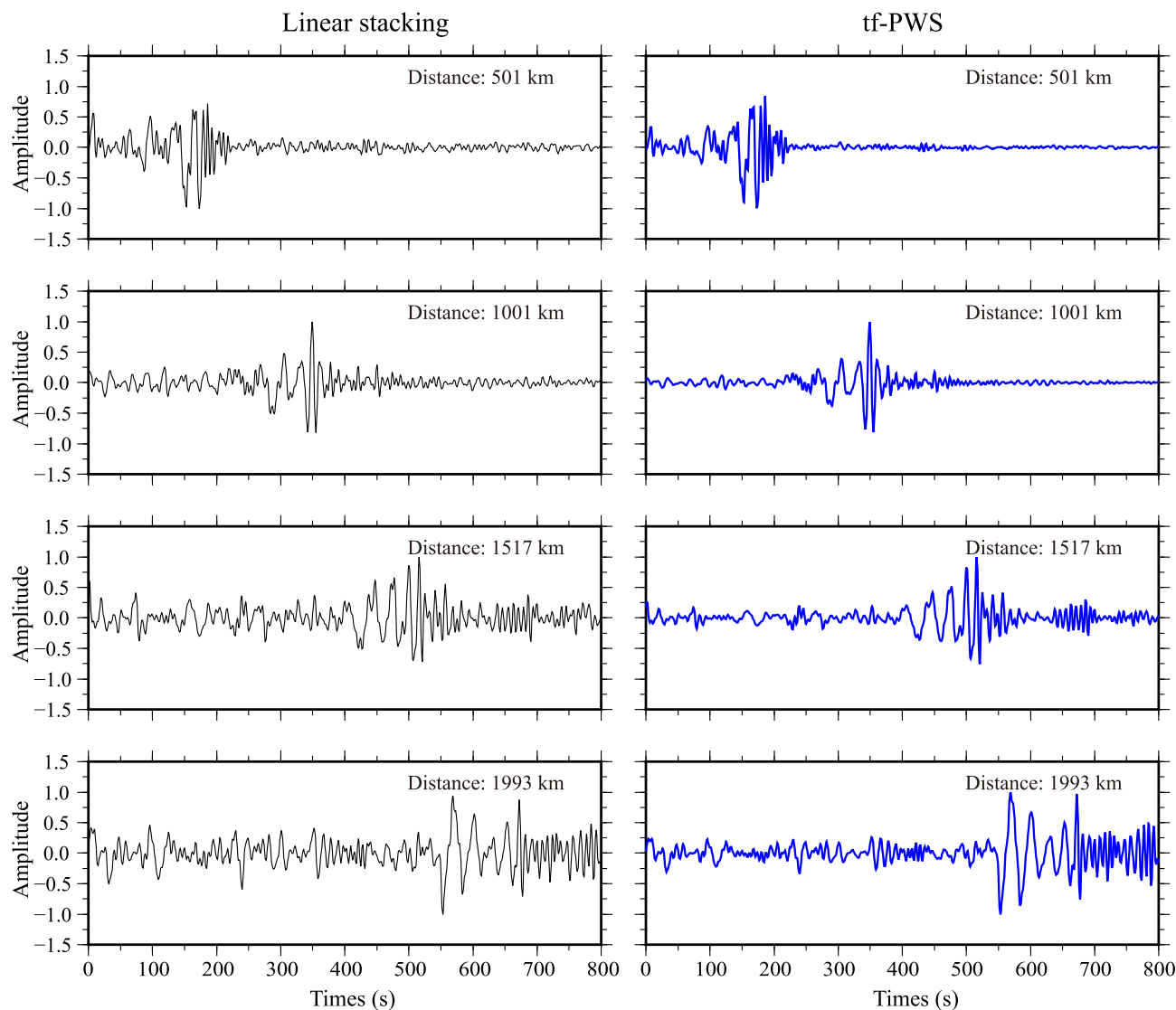


**Figure 8.** Examples showing a comparison of EGFs derived from the linear (left) and frequency IST-based tf-PWS (right) stacking methods. Note the relatively low noise levels in the tf-PWS EGFs shown on the right.

and reaches to its peak of 0.28 per cent at 50 s (solid green dots in Fig. 7b). It then decreases slowly and becomes nearly constant of 0.1 per cent at long periods (Fig. 7b). We note that the observed amplitude of the discrepancy related to the time IST-based tf-PWS is much smaller than that of the synthetic data (open red circles in Fig. 7a). This is likely due to the different amount of non-linear stacking involved in the synthetic and real data processing. Due to the large amount of USArray data, we employ a partial tf-PWS scheme in processing the real EGFs, that is, we first linearly stack 10 daily EGFs, and then use these 10-d EGFs to in the subsequent tf-PWS stacking. More specifically, the number of real EGFs used in the partial tf-PWS shown in Fig. 7(b) is only 63, while a total of 730 synthetic EGFs are employed in the full tf-PWS shown in Fig. 7(a). If we employ the same partial tf-PWS scheme in processing the synthetic data, the observed discrepancies are indeed much smaller than those derived from the full tf-PWS (solid circles in Fig. 7a).

Figs 9(a) and (b) show the histograms of the measured phase-velocity differences at six different periods for the frequency IST-based tf-PWS and time IST-based tf-PWS, respectively. For the

frequency IST-based tf-PWS, the differences measured at each period clearly follow the normal distribution with a mean close to zero and a standard deviation varying between 0.10 per cent and 0.21 per cent. However, for the time IST-based tf-PWS, the mean values at periods of 40–80 s are positive with a standard deviation varying between 0.17 per cent and 0.24 per cent.

Since the SNRs of the EGFs constructed from the tf-PWS method are much higher than those of the linear stacking, the tf-PWS stacks yield more effective measurements ( $\text{SNR} \geq 10$ , Fig. 10a). For example, at the period of 10 s, the effective measurements are 34 621 and 61 032 for the linear and tf-PWS stacks, respectively. These numbers are 3353 and 15 418 at 140 s. On average, we have 22 452 more measurements from the tf-PWS stacks, which is significant for surface wave tomography because increasing path density means better spatial resolution. In Fig. 10(b), we show the average SNR of the two types of stacked EGFs. At each period, the average SNR corresponding to tf-PWS is at least twice as large as that of the linear stacks.

Schimmel *et al.* (2017) showed that group and phase velocities can be extracted directly from the stacked elapse time spectra

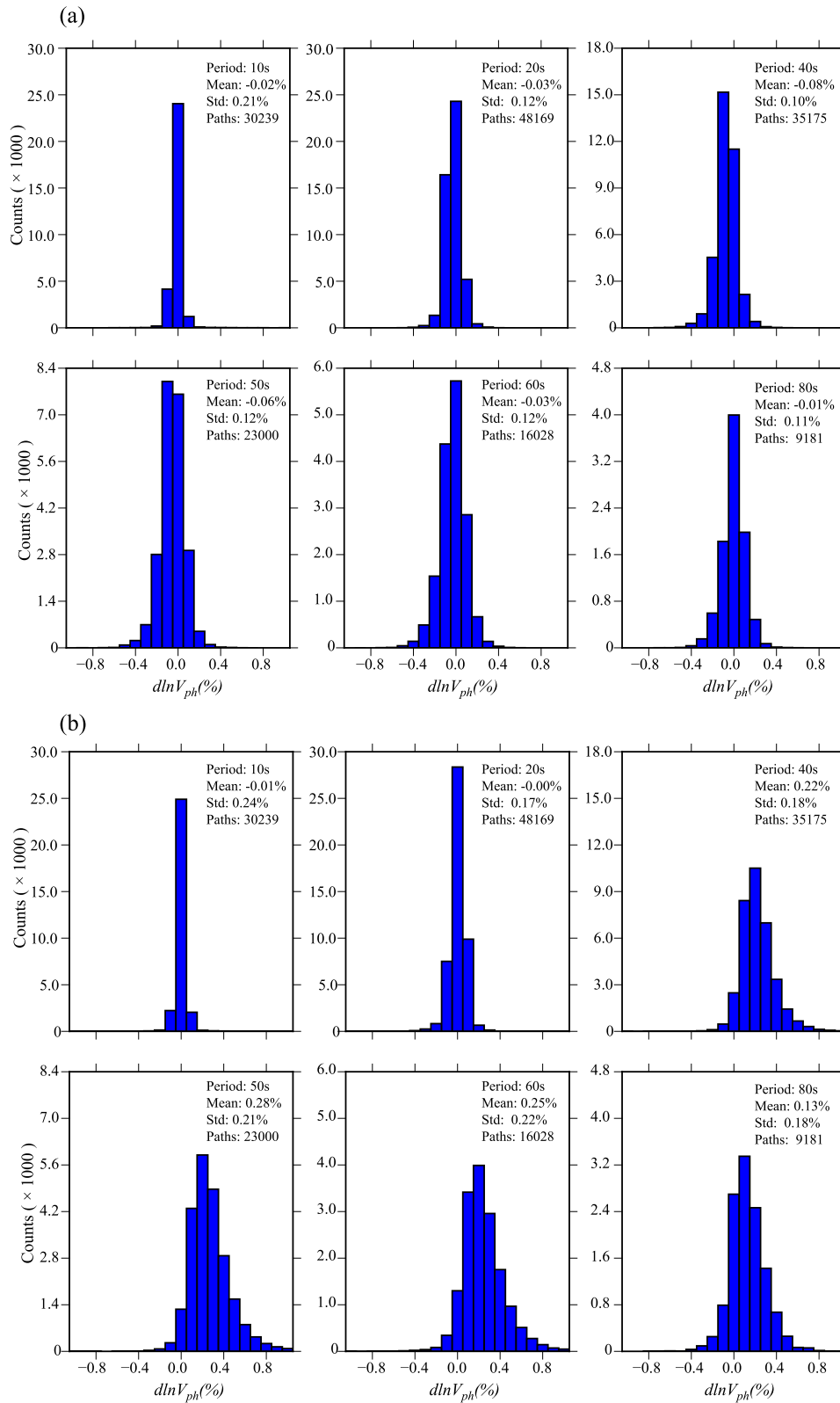


**Figure 9.** (a) Histograms showing the phase-velocity discrepancy between the frequency IST-based *tf-PWS* and linear stacks at six different periods: (a) 10 s, (b) 20 s, (c) 40 s, (d) 50 s, (e) 60 s and (f) 80 s. Note that they all roughly follow the normal distributions with nearly zero means and small standard deviations. (b) Similar to (a) but for the time IST-based *tf-PWS*.

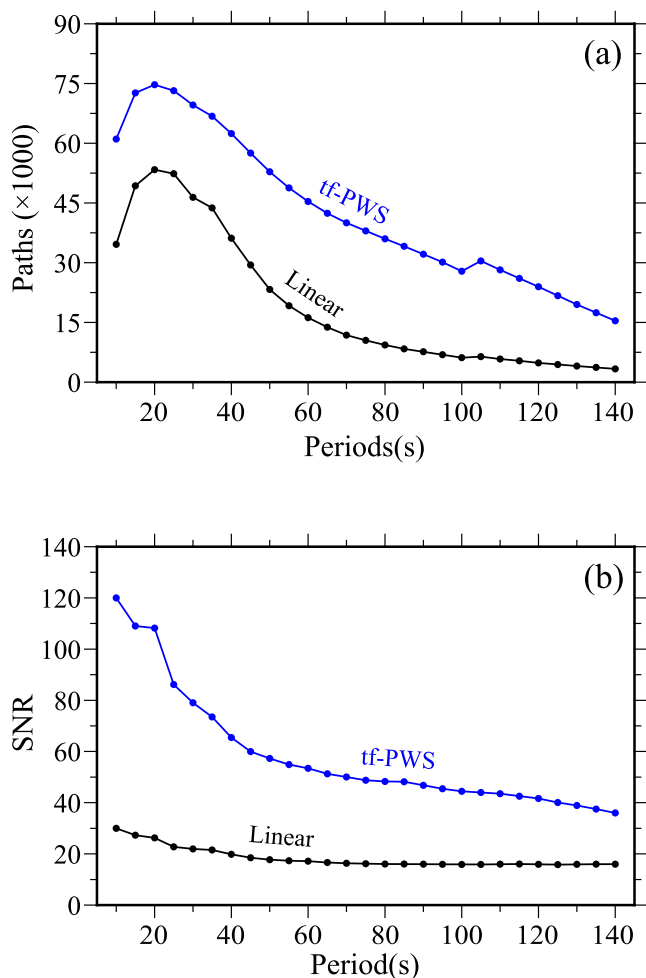


**Figure 10.** Number of effective measurements (a) and the average SNRs (b) are shown as functions of period, with black and blue representing those measured from the linear and frequency IST-based tf-PWS stacks, respectively.

$S(\tau, f)$  without performing an IST. Consequently, the systematic errors corresponding to the time IST-based tf-PWS can be avoided for conventional surface wave tomography (e.g. Yang *et al.* 2007) that relies on phase velocity, not waveform data. However, we argue here that constructing high SNR EGFs is still a valuable practice for many reasons. For example, adjoint tomography directly matches EGFs with 3-D synthetics (e.g. Chen *et al.* 2014), which requires time-domain EGFs. Meanwhile, EGFs are also widely used in time-lapse seismic imaging to detect velocity changes. In this case, time-series waveform data are also needed. Therefore, we believe that an accurate IST is still valuable to construct high SNR EGFs. Along this line, the phase coherence concept of the tf-PWS is worth exploring with any other analytic time–frequency representation and their respective inverse transforms that can yield more computational efficiency.

## 5 CONCLUSIONS

We investigate the feasibility of using the tf-PWS technique to construct EGFs for surface wave analysis. Through extensive numeric tests with both synthetic and real data, we reach the following conclusions: (1) tf-PWS has superior power in raising SNR, which has

significant advantages in detecting body waves, monitoring temporal changes in subsurface velocity and raising spatial resolution of surface wave tomography; (2) waveform distortion introduced by the frequency IST-based tf-PWS is very minor, and has almost negligible effects ( $<0.1$  per cent bias) on the measured phase velocities; (3) for unknown reasons the time IST-based tf-PWS tends to cause much larger waveform distortion than the frequency IST-based tf-PWS does. The former can introduce as much as 0.4 per cent systematic errors to the phase velocities of the long periods. Therefore, frequency IST is preferred in implementing tf-PWS to create EGFs from ambient noise data.

## ACKNOWLEDGEMENTS

We would like to thank the IRIS data centre for providing the TA station data, and Alan Levander from Rice for helpful discussion. We also thank the editor, Dr Martin Schimmel, and two anonymous reviewers for their constructive comments and suggestions, which significantly improved the quality of this paper. GL and FN are supported by NSFC 41274099 and NSF EAR-1547228. YY and XJ are supported by an ARC DP120103673 and Future Fellowship FT130101220. This is contribution 1029 from the ARC Centre of Excellence for Core to Crust Fluid Systems (<http://www.cafs.mq.edu.au>) and 1189 in the GEMOC Key Centre (<http://www.gemoc.mq.edu.au>).

## REFERENCES

- Baig, A.M., Campillo, M. & Brenguier, F., 2009. Denoising seismic noise cross correlations, *J. geophys. Res.*, **114**(B8), doi:10.1029/2008JB006085.
- Bensen, G.D. *et al.*, 2007. Processing seismic ambient noise data to obtain reliable broad-band surface wave dispersion measurements, *Geophys. J. Int.*, **169**(3), 1239–1260.
- Brenguier, F., Shapiro, N.M., Campillo, M., Ferrazzini, V., Duputel, Z., Coutant, O. & Nercessian, A., 2008. Towards forecasting volcanic eruptions using seismic noise, *Nature Geosci.*, **1**(2), 126–130.
- Chen, M., Huang, H., Yao, H., Van Der Hilst, R. & Niu, F., 2014. Low wave speed zones in the crust beneath SE Tibet revealed by ambient noise adjoint tomography, *Geophys. Res. Lett.*, **41**(2), 334–340.
- Cheng, X., Niu, F. & Wang, B., 2010. Coseismic velocity change in the rupture zone of the 2008 Mw 7.9 Wenchuan earthquake observed from ambient seismic noise, *Bull. seism. Soc. Am.*, **100**(5B), 2539–2550.
- Dziewonski, A.M., Bloch, S. & Landisman, M., 1969. A technique for the analysis of transient seismic signals, *Bull. seism. Soc. Am.*, **59**, 427–444.
- Grêt, A., Snieder, R., Aster, R.C. & Kyle, P.R., 2005. Monitoring rapid temporal change in a volcano with coda wave interferometry, *Geophys. Res. Lett.*, **32**, L06304, doi:10.1029/2004GL021143.
- Herrmann, R.B., 1973. Some aspects of band-pass filtering of surface waves, *Bull. seism. Soc. Am.*, **63**(2), 663–671.
- Herrin, E.E. & Goforth, T.T., 1977. Phase-matched filters: application to the study of Rayleigh Waves, *Bull. seism. Soc. Am.*, **67**, 1259–1275.
- Herrmann, R.B. & Ammon, C.J., 2004. Surface waves, receiver functions and crustal structure, in *Computer Programs in Seismology*, Version 3.30 [electronic], Available at: [http://www.eas.slu.edu/eqc/eqc\\_cps/CPS/CPS330/cps330c.pdf](http://www.eas.slu.edu/eqc/eqc_cps/CPS/CPS330/cps330c.pdf), last accessed 14 July 2011.
- Kanasewich, E.R., Hemmings, C.D. & Alpaslan, T., 1973. Nth-root stack nonlinear multichannel filter, *Geophysics*, **38**(2), 327–338.
- Kazemi, K., Amirian, M. & Dehghani, M.J., 2014. The S-transform using a new window to improve frequency and time resolutions, *SIWIP*, **8**(3), 533–541.
- Levshin, A.L., Yanovskaya, T.B., Lander, A.V., Bukchin, B.G., Barmin, M.P., Ratnikova, L.I. & Its, E.N., 1989. *Seismic Surface Waves in a Laterally Inhomogeneous Earth*, ed. Keilis-Borok, V.I., Kluwer, Norwell, MA.

- Levshin, A.L. & Ritzwoller, M.H., 2001. Automated detection, extraction, and measurement of regional surface waves, *Pure appl. geophys.*, **158**(8), 1531–1545.
- Li, D. & Castagna, J., 2013. Modified S-transform in time-frequency analysis of seismic data, in *83rd Annual International Meeting, SEG, Expanded Abstracts*, pp. 4629–4634.
- Li, G., Chen, H., Niu, F., Guo, Z., Yang, Y. & Xie, J., 2016. Measurement of Rayleigh wave ellipticity and its application to the joint inversion of high-resolution S wave velocity structure beneath northeast China, *J. geophys. Res.*, **121**, doi:10.1002/2015JB012459.
- Liu, Y., Niu, F., Chen, M. & Yang, W., 2017. 3-D crustal and uppermost mantle structure beneath NE China revealed by ambient noise adjoint tomography, *Earth planet. Sci. Lett.*, **461**, 20–29.
- Lin, F.-C., Tsai, V.C. & Schmandt, B., 2014. 3-D crustal structure of the western United States: application of Rayleigh-wave ellipticity extracted from noise cross-correlations, *Geophys. J. Int.*, **198**(2), 656–670.
- Mansinha, L., Stockwell, R.G., Lowe, R.P., Eramian, M. & Schincariol, R.A., 1997. Local S-spectrum analysis of 1-D and 2-D data, *Phys. Earth planet. Inter.*, **103**(3–4), 329–336.
- Mcfadden, P.D., Cook, J.G. & Forster, L.M., 1999. Decomposition of gear vibration signals by the generalised S transform, *Mech. Syst. Signal Process.*, **13**(5), 691–707.
- Muirhead, K.J., 1968. Eliminating false alarms when detecting seismic events automatically, *Nature*, **217**(5128), 533–534.
- Niu, F. & Chen, Q., 2008. Seismic evidence for distinct anisotropy in the innermost inner core, *Nature Geosci.*, **1**(10), 692–696.
- Pinnegar, C.R. & Eaton, D.W., 2003. Application of the S transform to prestack noise attenuation filtering, *J. geophys. Res.*, **108**(B9), doi:10.1029/2002JB002258.
- Schimmel, M. & Paulssen, H., 1997. Noise reduction and detection of weak, coherent signals through phase-weighted stacks, *Geophys. J. Int.*, **130**(2), 497–505.
- Schimmel, M. & Gallart, J., 2005. The inverse S-transform in filters with time-frequency localization, *IEEE Trans. Signal Process.*, **53**(11), 4417–4422.
- Schimmel, M. & Gallart, J., 2007. Frequency-dependent phase coherence for noise suppression in seismic array data, *J. geophys. Res.*, **112**, B04303, doi:10.1029/2006JB004680.
- Schimmel, M., Stutzmann, E. & Gallart, J., 2011. Using instantaneous phase coherence for signal extraction from ambient noise data at a local to a global scale, *Geophys. J. Int.*, **184**(1), 494–506.
- Schimmel, M., Stutzmann, E. & Ventosa, S., 2017. Measuring group velocity in seismic noise correlation studies based on phase coherence and resampling strategies, *IEEE Trans. Geosci. Remote Sens.*, **55**(4), 1–8.
- Sens-Schönfelder, C. & Wegler, U., 2006. Passive image interferometry and seasonal variations of seismic velocities at Merapi Volcano, Indonesia, *Geophys. Res. Lett.*, **33**(21), doi:10.1029/2006GL027797.
- Simon, C., Ventosa, S., Schimmel, M., Heldring, A., Danobeitia, J.J., Gallart, J. & Manuel, A., 2007. The S-transform and its inverses: side effects of discretizing and filtering, *IEEE Trans. Signal Process.*, **55**(10), 4928–4937.
- Shapiro, N.M., 2005. High-resolution surface-wave tomography from ambient seismic noise, *Science*, **307**(5715), 1615–1618.
- Stockwell, R.G., Mansinha, L. & Lowe, R.P., 1996. Localization of the complex spectrum: the S transform, *IEEE Trans. Signal Process.*, **44**(4), 998–1001.
- Stockwell, R.G., 2007. A basis for efficient representation of the S-transform, *Digital Signal Process.*, **17**(1), 371–393.
- Yang, Y., Ritzwoller, M.H., Levshin, A.L. & Shapiro, N.M., 2007. Ambient noise Rayleigh wave tomography across Europe, *Geophys. J. Int.*, **168**(1), 259–274.
- Yang, Y., Ritzwoller, M.H., Zheng, Y., Shen, W., Levshin, A.L. & Xie, Z., 2012. A synoptic view of the distribution and connectivity of the mid-crustal low velocity zone beneath Tibet, *J. geophys. Res.*, **117**(B4), doi:10.1029/2011JB008810.

## APPENDIX: TIME AND FREQUENCY INVERSE S TRANSFORMS OF THE FILTERED ELAPSE TIME SPECTRA $S_{\text{pws}}(\tau, f)$

The filtered elapse time spectra corresponding to tf-PWS can be written as:

$$S_{\text{pws}}(\tau, f) = |c_{\text{ps}}(\tau, f)|^v S_{\text{linear}}(\tau, f) \quad (\text{A1})$$

And here we assign  $v = 1$  and let  $S_{\text{linear}}(\tau, f)$  denotes the S transform of the linearly stacked part:

$$S_{\text{linear}}(\tau, f) = \frac{1}{N} \sum_{j=1}^N S_j(\tau, f) \quad (\text{A2})$$

The inverse Fourier transform of eq. (A2) takes the following form:

$$x'(\tau, t) = \int_{-\infty}^{+\infty} \frac{k\sqrt{2\pi}}{|f|} S_{\text{linear}}(\tau, f) c_{\text{ps}}(\tau, f) e^{i2\pi f t} df \quad (\text{A3})$$

Combining with eq. (10) and setting  $\tau = t$ , we can get the following equation from eq. (A3):

$$\begin{aligned} x'(t, t) &= \int_{-\infty}^{+\infty} \int_{-\infty}^{+\infty} u(t') e^{-\frac{f^2(t-t')^2}{2k^2}} e^{i2\pi f(t-t')} dt' \cdot c_{\text{ps}}(t, f) df \\ &= \int_{-\infty}^{+\infty} c_{\text{ps}}(t, f) \int_{-\infty}^{+\infty} u(t') e^{-\frac{f^2(t-t')^2}{2k^2}} e^{i2\pi f(t-t')} dt' df \end{aligned} \quad (\text{A4})$$

In eq. (A4), the inner integration can be seen as the convolution of  $u(t)$  with  $y(t) = e^{-\frac{f^2 t^2}{2k^2}} e^{i2\pi f t}$ , and as the Fourier transform of the  $y(t)$  is:

$$Y(v) = \frac{k\sqrt{2\pi}}{|f|} e^{-\frac{2\pi^2 k^2 (v-f)^2}{f^2}} \quad (\text{A5})$$

Then, eq. (A4) can evolve into:

$$\begin{aligned} x'(t, t) &= \int_{-\infty}^{+\infty} c_{\text{ps}}(t, f) \int_{-\infty}^{+\infty} U(v) \frac{k\sqrt{2\pi}}{|f|} e^{-\frac{2\pi^2 k^2 (v-f)^2}{f^2}} e^{i2\pi v t} dv df \\ &= \int_{-\infty}^{+\infty} U(v) \int_{-\infty}^{+\infty} c_{\text{ps}}(t, f) \frac{k\sqrt{2\pi}}{|f|} e^{-\frac{2\pi^2 k^2 (v-f)^2}{f^2}} df e^{i2\pi v t} dv. \end{aligned} \quad (\text{A6})$$

If we assume that the weight function  $c_{\text{ps}}(t, f)$  can be decomposed into two real functions:

$$c_{\text{ps}}(t, f) = f(t)g(f) \quad (\text{A7})$$

Then, eq. (A6) can be written as:

$$x'(t, t) = f(t) \int_{-\infty}^{+\infty} U(v) \int_{-\infty}^{+\infty} g(f) \frac{k\sqrt{2\pi}}{|f|} e^{-\frac{2\pi^2 k^2 (v-f)^2}{f^2}} df e^{i2\pi v t} dv \quad (\text{A8})$$

Here, we denote the inner integral in eq. (A8) as  $H(v)$ :

$$H(v) = \int_{-\infty}^{+\infty} g(f) \frac{k\sqrt{2\pi}}{|f|} e^{-\frac{2\pi^2 k^2 (v-f)^2}{f^2}} df \quad (\text{A9})$$

Then, eq. (A8) can be rewritten as:

$$x'(t, t) = f(t) \int_{-\infty}^{+\infty} U(v) H(v) e^{i2\pi v t} dv = f(t) \cdot \{u(t) * h(t)\}, \quad (\text{A10})$$

where  $h(t)$  is the time sequence with a spectrum of  $H(\nu)$ , which is real function based on eq. (A9). If we take the Fourier transform of eq. (A10), we can get the Fourier spectrum of the filtered data as:

$$\mathfrak{F}^{-1}\{x'(t, t)\} = F(f) * \{U(f) \cdot H(f)\} \quad (\text{A11})$$

In eq. (A11), the  $F(f)$  is the Fourier spectrum of function  $f(t)$ . As  $H(f)$  is a real function, it does not change the phase of the function  $U(f)$ . However, since  $F(f)$  is generally a complex function, it does affect the phase spectrum of  $U(f)$ . Therefore, the phase of the filtered data experiences a frequency-dependent change.

On the other hand, the frequency IST of the tf-PWS spectra can be written as:

$$\begin{aligned} u_{\text{pws}}(t) &= \int_{-\infty}^{+\infty} \int_{-\infty}^{+\infty} |c_{\text{ps}}(\tau, f)|^v S_{\text{linear}}(\tau, f) d\tau e^{i2\pi ft} df \\ &= \int_{-\infty}^{+\infty} U_{\text{pws}}(f) e^{i2\pi ft} df \end{aligned} \quad (\text{A12})$$

where  $U_{\text{pws}}(f)$  is the Fourier spectrum of the phase-weighted stacked signal, and can be written as

$$U_{\text{pws}}(f) = \int_{-\infty}^{+\infty} |c_{\text{ps}}(\tau, f)|^v S_{\text{linear}}(\tau, f) d\tau. \quad (\text{A13})$$

Here,  $|c_{\text{ps}}(\tau, f)|^v$  is a positive-real function, and  $U_{\text{pws}}(f)$  and  $S_{\text{linear}}(\tau, f)$  are complex functions. If we express eq. (A13) in polar form and take the natural logarithm of both sides:

$$\begin{aligned} \ln |U_{\text{pws}}(f)| + i\Phi_{U_{\text{pws}}}(f) \\ = \int_{-\infty}^{+\infty} \{v \ln |c_{\text{ps}}(\tau, f)| + \ln |S_{\text{linear}}(\tau, f)| + i\Phi_{S_{\text{linear}}}(\tau, f)\} d\tau \end{aligned} \quad (\text{A14})$$

Therefore, the phases of the frequency IST-based tf-PWS and the linear stacked signals are the same.

$$\Phi_{U_{\text{pws}}}(f) = \int_{-\infty}^{+\infty} \Phi_{S_{\text{linear}}}(\tau, f) d\tau = \Phi_U(f) \quad (\text{A15})$$